INSTITUTE OF PHYSICS PUBLISHING and INTERNATIONAL ATOMIC ENERGY AGENCY NUCLEAR FUSION

Nucl. Fusion **45** (2005) 1–9 doi:10.1088/0029-5515/45/5/...

Short laser pulse induced generation of hot electrons and their anomalous stopping in overdense plasmas

S. Sengupta[1], A.S. Sandhu[2], G.R. Kumar[2], A. Das[1] and P.K. Kaw[1]

[1] Institute for Plasma Research, Bhat, Gandhinagar 382 428, India
[2] Tata Institute of Fundamental Research, 1 Homi Bhabha Road, Mumbai 400 005, India

Received 3 December 2004, accepted for publication 1 August 2005
Published
Online at stacks.iop.org/NF/45

Abstract

In the fast ignition (FI) scheme of inertial confinement fusion, the igniter pulse falls on a precompressed overdense target and hence is unable to penetrate it. Thus, for the task of hot spot generation one has to rely on energetic electrons which are produced by the laser pulse at the critical surface. These electrons subsequently move towards the target core and deposit their energy in a sufficiently localized region. It is thus clear that the production of hot electrons by the incident sub-picosecond laser pulse at the critical surface and their subsequent transport in the overdense plasma region are the two main physics issues which are of relevance to the FI scheme. An experimental study and theoretical analysis which may be of relevance to these two issues are presented here. The study shows that the production of energetic electrons occurs through the wave breaking of plasma waves excited at the critical surface by the incident laser beam. Further, the propagation of hot electrons through the overdense region is influenced by electrostatically induced and/or by turbulence induced anomalous resistivity.

PACS numbers: 52.57.Kk

1. Introduction

AQ1

In the inertial confinement fusion (ICF) scheme of thermonuclear fusion, a spherically symmetric deuterium–tritium (D–T) capsule is imploded to $\sim 10^3$ times its solid density with the help of a nanosecond duration laser pulse. In the conventional ICF scheme the same laser pulse is used to heat the compressed target core to temperatures of the order of ~ 10 keV (required for initiating fusion reactions). The growth rate of hydrodynamic instabilities being much smaller than a nanosecond, these (Rayleigh–Taylor etc) begin to develop even before the target reaches its fully compressed state. The development of these instabilities is detrimental to initiating fusion reactions, as they mix up the cold and hot fuels in the target. In the conventional method one avoids the development of these instabilities by imposing stringent requirements on implosion symmetry. The target design as well as the laser illumination should have perfect spherical symmetry. This being an idealization, one ends up requiring very high laser energies to counter the adverse role of the instabilities, to an extent that they are unavoidable. Recently, a variant to the conventional ICF scheme known as fast ignition (FI) scheme has been introduced which relaxes most of the above-mentioned stringent requirements. In this scheme the task of compression is separated from that of heating the target. In the first stage of FI the target is compressed without heating, using a series of slow shocks generated by a nanosecond duration laser pulse. In the second stage, a sub-picosecond petawatt laser pulse is utilized for creating a hot spot inside the target. The target being overdense, this laser pulse is unable to penetrate it; instead its energy is absorbed at the critical surface resulting in the generation of energetic electrons. One relies on these energetic electrons for the production of a hot spot inside the target. It is therefore essential that these fast electrons stop within the target. Hence, the two main physics issues in the FI scheme are viz. the mechanism of hot electron production at the critical surface and the transport of these electrons through the overdense region of the target. A proper understanding of these two issues is desirable. The results of some recent experiments have demonstrated the potential of the FI scheme, by showing enhancement in neutron yield produced during fusion reactions [1, 2]. In this paper we present results from two experiments which may throw light on the physics concerning the aforementioned issues. The experimental work, although carried out at modest intensities $\sim 10^{20}$ W m^{-2}, can possibly throw light on the physical mechanisms associated with the production and propagation of energetic electrons. In section 2, the experimental work and theoretical analysis related to the production of hot electrons are presented. Section 3 deals with studies associated with the transport

JNL: NF PIPS: 190712 TYPE: PAP TS: NEWGEN DATE: 11/8/2005 EDITOR: BA

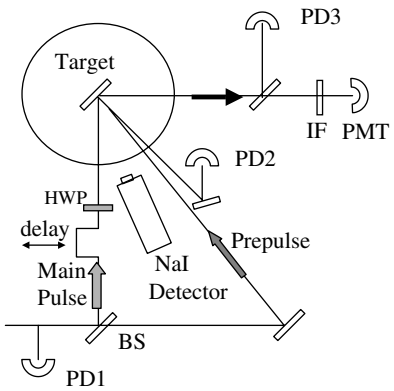

Figure 1. A schematic showing the experimental set-up for the hot electron generation experiments.

characteristics of energetic electrons. Finally, we provide a summary and conclusion of our work in section 4.

2. Generation of hot electrons

As mentioned in the previous section, during the ignition phase of the FI scheme, the petawatt laser which is incident on the precompressed target is unable to propagate inside the overdense plasma, its density being five orders of magnitude higher than the critical density. Therefore most of the laser energy is absorbed at the surface. A simple estimate for a sub-picosecond laser with intensity of the order of $\sim 10^{23}\,\mathrm{W\,m^{-2}}$ shows that the density scale length L due to the surface expansion of the target can be greater than or equal to the quiver amplitude x_{osc} of the electrons in the laser electric field. This indicates that in addition to vacuum heating, resonance absorption of the laser energy may also take place. In this work, we have specifically looked at resonance absorption scheme and its role in the production of hot electron current.

2.1. Experimental results

In figure 1, we show a schematic of the experimental arrangement used for studying hot electron generation. As shown in the figure, here we employ a prepulse of intensity $\sim 2 \times 10^{18}\,\mathrm{W\,m^{-2}}$ for the purpose of plasma formation. The prepulse is normally incident on the target. A second laser pulse (main pulse in figure 1) falls on the target after a specified time delay τ. This pulse is p polarized and is incident obliquely at an angle of 45° with respect to the target normal. The intensity of the main pulse is $\sim 10^{20}\,\mathrm{W\,m^{-2}}$, its duration is 100 fs and its wavelength is 800 nm. Three different measurements, namely the reflectivity of the main pulse, the efficiency of second harmonic generation and hard x-ray emission are carried out as a function of time delay τ between the prepulse and the main pulse. Figures 2 and 3, respectively, show the hard x-ray yield over 30–300 keV range and the second harmonic generation efficiency $\eta \propto I(2\omega)/I^2(\omega)$ as a function of time delay (bottom axis in both cases). In both the plots the data are normalized with respect to the yield obtained without prepulse (i.e. no preformed plasma). The jagged line in the plot corresponds to the experimental data and the continuous curve represents a fit obtained on the basis of our proposed physical mechanism. The theoretical details of the fit are described in the next subsection. The most notable feature of these plots is the observed dip in the second harmonic efficiency around ∼24 ps, which occurs nearly at the same point at which the hard x-ray emission maximizes. The second harmonic efficiency at this point dips to half of its maximum value, whereas the hard x-ray yield is enhanced by two orders of magnitude as compared with its baseline value. The enhancement of hard x-ray yield around ∼24 ps is a strong indicator of copious generation of hot electrons. A comparison of hot electron temperatures (obtained with the help of spectrally resolved hard x-ray yield) without and with a time delay of ∼24 ps (the top and bottom plot, respectively, in figure 4) shows a significant high temperature component in the latter case (as can be seen from the statistical weights). This provides clear evidence for the presence and hence the generation of hot electrons. About the second harmonic generation, we note that it was found to be specular in our experiments, which indicates that it is generated by electron plasma waves produced by linear conversion mechanism like resonance absorption [3, 4].

We have also measured the reflectivity of the main pulse, which is shown in figure 5. The reflectivity data also dips around the time delay of ∼24 ps (around the same point where the hard x-ray yield maximizes and the second harmonic generation efficiency dips) indicating that maximum absorption of laser energy takes place around this time delay. The trends shown by the three measurements reaffirm the existence of a consistent simple physical mechanism, which we qualitatively outline here. The delay between the prepulse and the main pulse basically determines the density scale length. As the time delay increases, the plasma formed by the prepulse gets more time for expansion. Thus there exists a one-to-one relationship between τ and the plasma scale length $(L/\lambda)_{\mathrm{cr}}$. The decreasing reflectivity of the main pulse bears testimony to the fact that as the scale length increases, the resonance absorption increases; it maximizes around 24 ps where the reflectivity is minimum. Beyond this point the rise in reflectivity points at decreasing absorption. We propose that around the peak of resonance absorption large amplitude electrostatic plasma waves are excited which meet the wave breaking criteria and thus undergo strong nonlinear damping, thereby resulting in copious production of hot electrons. The x-ray yield, which depends on the intensity of hot electrons, thereby maximizes at this point. On the other hand, the second harmonic generation which depends on the existence of plasma wave shows a dip. In the next subsection we present supporting evidence to this physical scenario by providing consistent quantitative fit to the experimental data for both x-ray emission and second harmonic generation efficiency using estimates for $\nu_{\mathrm{eff}}/\omega$ (ν_{eff} being the effective collision frequency) from the reflectivity data.

2.2. Theoretical modelling and analysis of data

We now present an analysis of the experimental results which makes a strong case for resonance absorption and wave breaking as physical mechanisms responsible for hot electron current generation and the second harmonic emission. Our analysis is based on models for the x-ray yield and the second harmonic generation efficiency. We model the x-ray

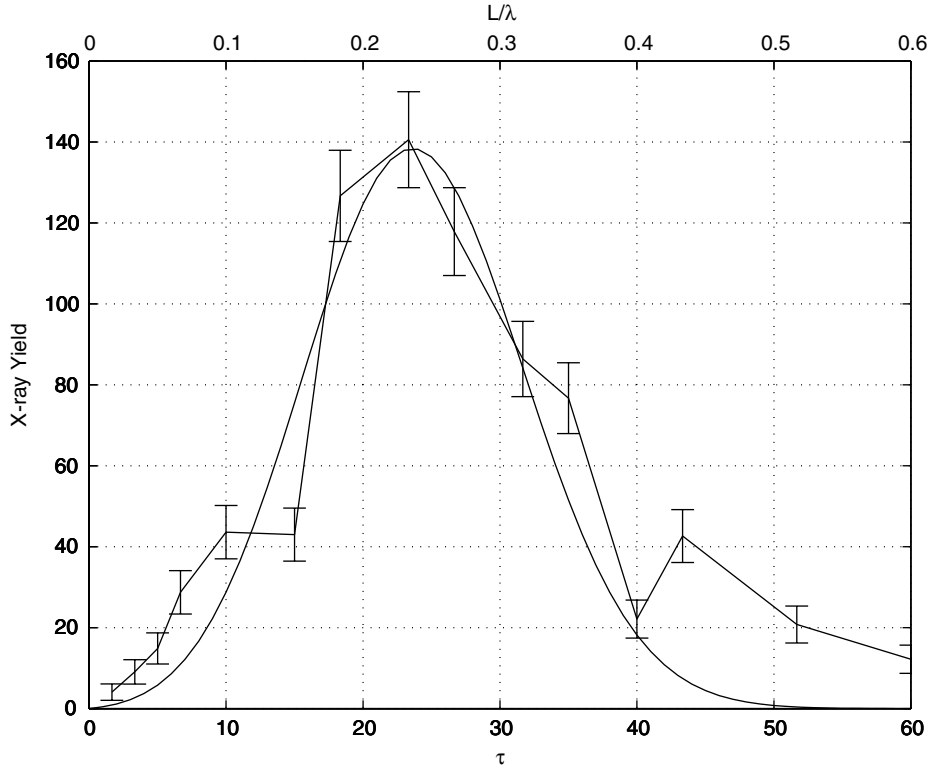

Figure 2. X-ray yield versus the time delay τ between the prepulse and the main pulse. The jagged line connects the experimental points. The continuous curve shows the theoretical fit.

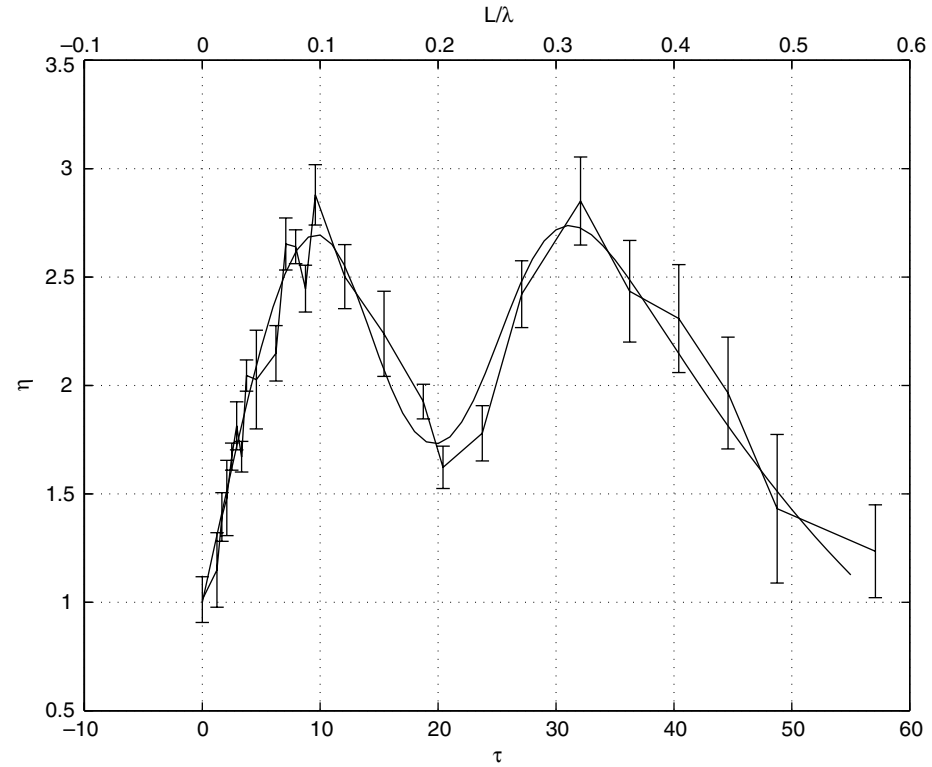

Figure 3. The second harmonic generation efficiency versus τ, the delay between the prepulse and the main pulse.

yield as a quantity Y which is taken to be proportional to the intensity of the absorbed light $I_{\rm abs} = \int_0^\infty \nu_{\rm eff} E_z^2/8\pi \, {\rm d}z$, where $\nu_{\rm eff}$ is the effective rate at which energy is drained out of the plasma wave through linear/nonlinear processes and E_z is the electric field associated with the plasma wave. For $\nu_{\rm eff}/\omega \to 0$ (linear processes), $E_z \sim 1/\epsilon \sim 1/(\nu_{\rm eff}/\omega)$ and the width of the resonance region is proportional to $\nu_{\rm eff}$, resulting in $I_{\rm abs}$ becoming independent of $\nu_{\rm eff}$. This implies that the intensity of the absorbed light is independent of the process of absorption, a fact which is well known in resonance

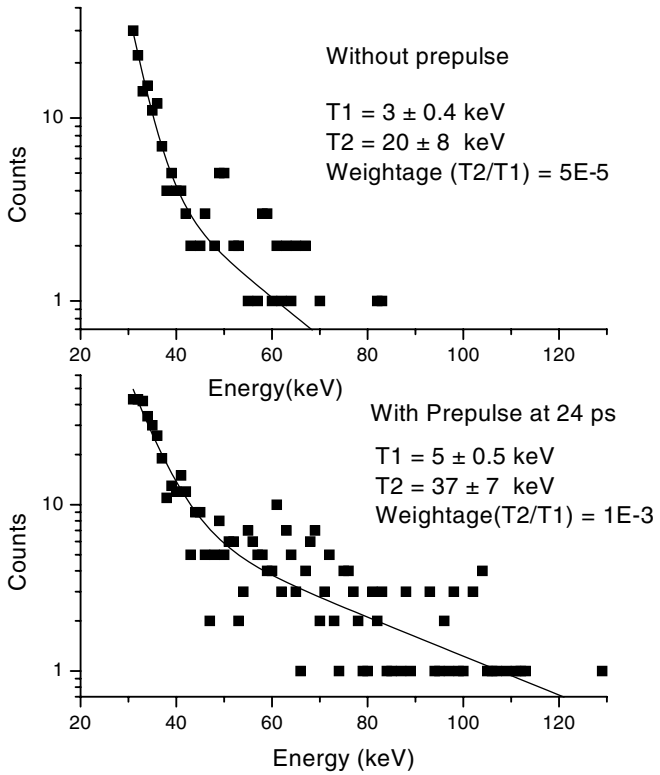

Figure 4. The top and bottom plots, respectively, show spectrally resolved x-ray yield in the absence of any prepulse and in the presence of prepulse with the main pulse following after 24 ps. The continuous curve in the two subplots show fit to the hot electron temperature. It can be seen that the hot electron temperature is higher in the presence of prepulse.

absorption theory. In general, however, for nonlinear processes intensity of the absorbed light is dependent on the process of absorption. This is because the amplitude of the excited plasma wave, as it approaches the resonance region, instead of increasing as $E_z \sim 1/\epsilon$, gets clamped to the value dictated by the wave breaking condition $k_p e E_{WB}/(m\omega_p^2) \sim 1$, where $k_p \sim (\lambda_D^2 L)^{-1/3}$ is the wavenumber of the plasma wave. Therefore, the absorption integral can be written as

$$I_{abs} \approx \int_0^l \nu_{eff} \frac{E_z^2}{8\pi} dz + \int_l^\infty \nu_{eff} \frac{E_{WB}^2}{8\pi} dz, \qquad (1)$$

where $E_{WB} \sim m\omega_p^2(\lambda_D^2 L)^{1/3}/e$ and 'l' is the point of initiation of wave breaking. We believe that it is the second integral which contributes maximally to the x-ray yield. We thus model the x-ray yield as

$$Y \propto \int_l^\infty \nu_{eff} \frac{E_{WB}^2}{8\pi} dz \approx \nu_{eff}(\lambda_D^2 L)^{1/3} \frac{E_{WB}^2}{8\pi}, \qquad (2)$$

where the range of integration is approximately taken as wavelength of the plasma wave near the resonant region. Thus

$$Y = A \left(\frac{L}{\lambda}\right)_{cr} f\left(\frac{L}{\lambda}\right)_{cr}, \qquad (3)$$

where A is some proportionality constant and $\nu_{eff} = f(L/\lambda)_{cr}$ is an unknown function of the argument.

For the second harmonic generation efficiency we use the model developed by Erokhin *et al* [6], which gives the scaling of second harmonic generation efficiency η with $(L/\lambda)_{cr}$ and $(\nu_{eff}/\omega)_{cr}$ as $\eta \propto \rho^2 \exp[-(b + d(\nu/\omega)_{cr})\rho]$. Here $\rho = 2\pi(L/\lambda)_{cr}$ and 'b' and 'd' are two constants of order unity. Thus the x-ray yield and the second harmonic generation efficiency both are functions of scale length $(L/\lambda)_{cr}$ and $(\nu_{eff}/\omega)_{cr}$. The reflectivity data of figure 5 serve two purposes. Firstly, from its minima and using the assumption of uniform plasma expansion velocity, the τ axis can be calibrated in terms of $(L/\lambda)_{cr}$. We use the condition for maximum resonance absorption to estimate the scale length. This is because the plasma scale length at which resonance absorption peaks is independent of the process of damping of the electrostatic wave (i.e. whether the wave damps through electron–ion collisions or through wave breaking, the scale length at which resonance absorption peaks remains the same [5]). The condition for maximum resonance absorption is given by $[2\pi(L/\lambda)_{cr}]^{1/3} \sin\theta \approx 0.8$, which implies that $(L/\lambda)_{cr} \approx 0.23$. The experimental data (keeping in view all the three measurements) provide enough evidence that maximum absorption occurs around $\tau \sim 24$ ps. This provides an estimate of the expansion velocity as $V_{exp} \approx 7.7 \times 10^3\,\mathrm{m\,s^{-1}}$. This estimate of plasma expansion velocity is very reasonable for the prepulse intensity of $2 \times 10^{18}\,\mathrm{W\,m^{-2}}$. Using this value of expansion velocity we calibrate the time delay τ axis in terms of density scale length $(L/\lambda)_{cr}$ which is represented by the top axis in figures 2, 3 and 5. Thus the reflectivity as a function of τ represents the experimentally measured value of reflectivity as a function of density scale length at the critical layer $(L/\lambda)_{cr}$. Secondly, the information provided by the reflectivity data is that of $(\nu_{eff}/\omega)_{cr}$ as a function of scale length $(L/\lambda)_{cr}$. For this purpose we numerically solve the wave equation for the magnetic field of a p polarized light propagating through an inhomogeneous plasma medium [7]. The inhomogeneity is represented by choosing a linear density profile for the plasma. Treating $(\nu_{eff}/\omega)_{cr}$ as a parameter in the numerical solution, the value of reflectivity is evaluated corresponding to different values of the scale length $(L/\lambda)_{cr}$. The parameter value of $(\nu_{eff}/\omega)_{cr}$ for which the numerically evaluated reflectivity matches with the experimental value is considered the correct estimate for $(\nu_{eff}/\omega)_{cr}$. Figure 6 shows a plot of such an estimate for $(\nu_{eff}/\omega)_{cr}$ as a function of $(L/\lambda)_{cr}$. The error bars in figure 6 correspond to those in the reflectivity curve in figure 5. Note that the estimated value of $(\nu_{eff}/\omega)_{cr} \sim 0.16$ at the maximum of resonance absorption is an order of magnitude higher than the classical value of ν_{eff}/ω estimated using electron–ion collisions at 100 eV, which is the typical bulk temperature in our experiments. Rewriting the wave breaking parameter using $k_p \sim 1/(\epsilon L)$, $\epsilon \sim \nu_{eff}/\omega$, we get [5, 6]

$$\frac{k_p e E_z}{m\omega_p^2} \sim 0.9 \frac{e E_{FS} \sin\theta}{mc\omega} \rho^{-7/6} \exp\left(-\frac{2}{3}\rho \sin^3\theta\right) \frac{1}{(\nu_{eff}/\omega)^2}, \qquad (4)$$

where E_{FS} is the free space electric field, $\rho = \omega L/c$ and θ is the angle of incidence. Using the experimentally measured value of $(\nu_{eff}/\omega)_{cr} \sim 0.16$ at $(L/\lambda)_{cr} \sim 0.23$, the wave breaking parameter turns out to be of order unity. This is a clear indication that the damping of electrostatic plasma wave in this regime is occurring via nonlinear wave breaking mechanism. We now use these estimated values of ν_{eff}/ω

AQ2

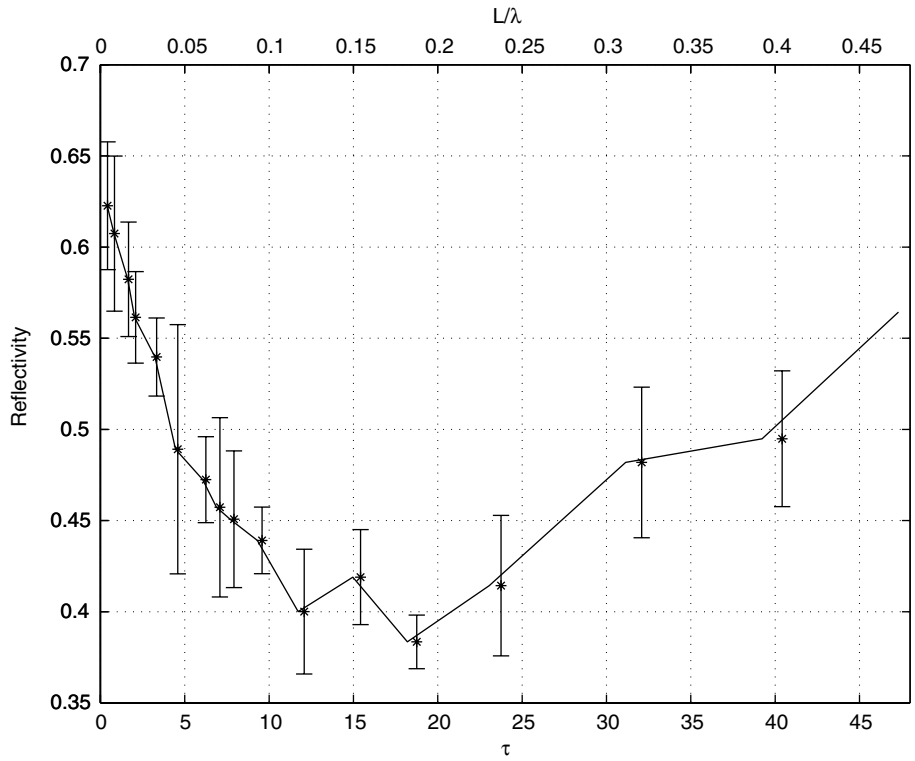

Figure 5. Reflectivity of the main pulse as a function of time delay.

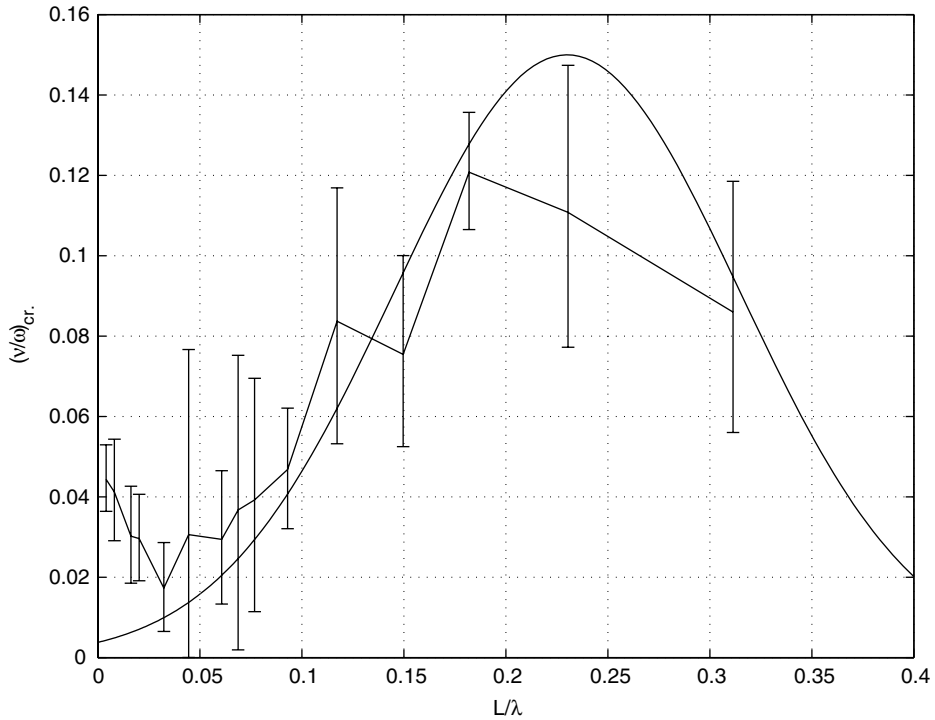

Figure 6. Estimated value of $(\nu_{\rm eff}/\omega)$ from the reflectivity data. The continuous curve is the plot of the analytical function which is used for representing the gross features.

as a function of scale length in the two models discussed earlier for the x-ray yield and the second harmonic generation efficiency. For this purpose we represent the gross behaviour of $(\nu_{\rm eff}/\omega)_{\rm cr}$ by a Gaussian function of the form $(\nu_{\rm eff}/\omega)_{\rm cr} = a\exp[-((L/\lambda)_{\rm cr} - c)^2/\omega^2]$ with $a = 0.16$, $c = 0.2$ and $w = 0.1$ (figure 6). This Gaussian profile of $(\nu_{\rm eff}/\omega)_{\rm cr}$, as a function of $(L/\lambda)_{\rm cr}$, captures the essence of resonance absorption and wave breaking physics. For small and large values of $(L/\lambda)_{\rm cr}$ the amplitude of the excited wave is low, and the rate at which energy is extracted out of the wave is also low. There exists an optimum value of $(L/\lambda)_{\rm cr}$ (for a fixed angle of incidence) for which the amplitude of the plasma wave is maximum [5], which for our laser intensities ($\sim 10^{20}\,{\rm W\,m^{-2}}$) can reach the wave breaking limit. The large value of $(\nu_{\rm eff}/\omega)_{\rm cr}$

around this optimum value of $(L/\lambda)_{cr}$ represents efficient conversion of wave energy into particle kinetic energy, which is a physical outcome of wave breaking. We now use this functional form in the models for Y and η. This generates the continuous curves of figures 2 and 3. It can be seen that a remarkably good fit to the measured experimental values is obtained by this process. This clearly shows the consistency of all the three kinds of data with the theory of resonance absorption and the wave breaking mechanism postulated for the hot electron generation. We believe that in the FI scenario too, as the igniter pulse is incident on a preformed overdense plasma, the same physical mechanism may be operative.

3. Hot electron transport

We now address the issue of the transport of hot electrons generated at the critical layer through the overdense region of the target. Clearly, as the hot electrons move inwards through the overdense region, space charge imbalances would be created. If the resistivity of the background plasma is small, a cold return electron current would immediately flow, thereby neutralizing any buildup of space charges. On the other hand, if the resistivity of the background plasma is high, there is no such neutralization of the space charge fields. In the latter case the hot electron current would immediately get inhibited by strong electrostatic fields. In the former case too there is stopping of hot electron current, but in this case the mechanism of stopping is altogether different. The forward and the return shielding currents, in this case, are amenable to the development of a host of instabilities. The Weibel, filamentation and coalescence instabilities are the first to occur, which lead to the formation of current channels in which the hot electrons flow in the core, and the outer cylindrical shell carries the return shielding current. It has been shown that such a configuration is unstable to sausage and kink-like electron magnetohydrodynamic instabilities [8–10]. Simulations suggest that the resulting electromagnetic turbulence may cause anomalous stopping of the hot electron current [11]. In this work we provide experimental evidence for both kinds of stopping mechanisms by studying the flow of hot electrons in a conducting (Al) and a resistive (BK7 glass) target. As the true value of resistivity of the dense core is unknown, we believe that in the FI scheme any one or a combination of both these stopping mechanisms for the hot electron current may be operative.

In the next subsection we discuss the experiments and the results. The subsequent subsection contains the details of the theoretical analysis of the experimental data.

3.1. Experimental results

As mentioned earlier, our objective is to study the transport of hot electrons in two different media having very different resistivities. For this purpose we have chosen BK7 glass, which is an insulator, and aluminium, which is a metal. To compare the transport of electrons, we need to employ an identical source of hot electrons in both the cases. We ensure this by coating a thin layer of aluminium ($\sim$0.5 μm thick) on the glass target. The experimentally measured hard x-ray emission obtained from these samples is shown in figure 7. The hot electron temperature obtained from the fit to the experimental data turns out to be identical ($\sim$30 keV) for the two cases as can be seen from figure 7. This shows that the electron source in both the cases can be treated as identical.

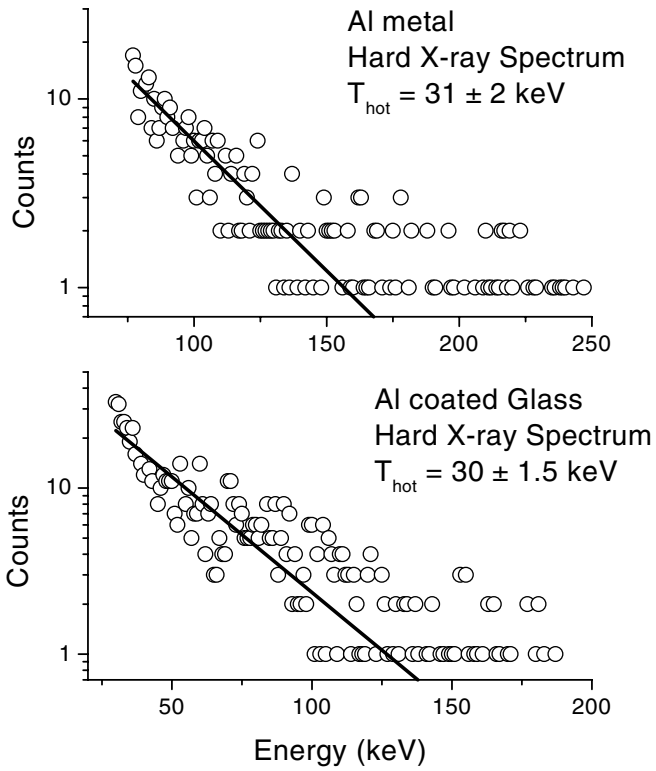

Figure 7. Spectrally resolved x-ray yield for aluminium and glass coated with aluminium are shown in the top and bottom plots of the figure. The solid lines show a fit for the hot electron temperature.

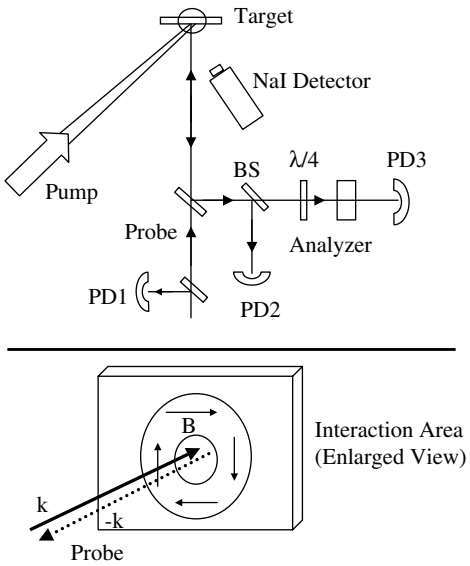

Figure 8. The schematic showing the experimental set-up for the hot electron transport experiments.

The schematic of the experimental set-up used for studying the transport properties of hot electrons is shown in figure 8. We now employ the basic technique of pump probe polarimetry to study the temporal evolution of quasi-static magnetic fields, which provide information on the propagation of hot electrons in the two targets. As shown in figure 8, a pump pulse is incident at an angle of 45° with respect to

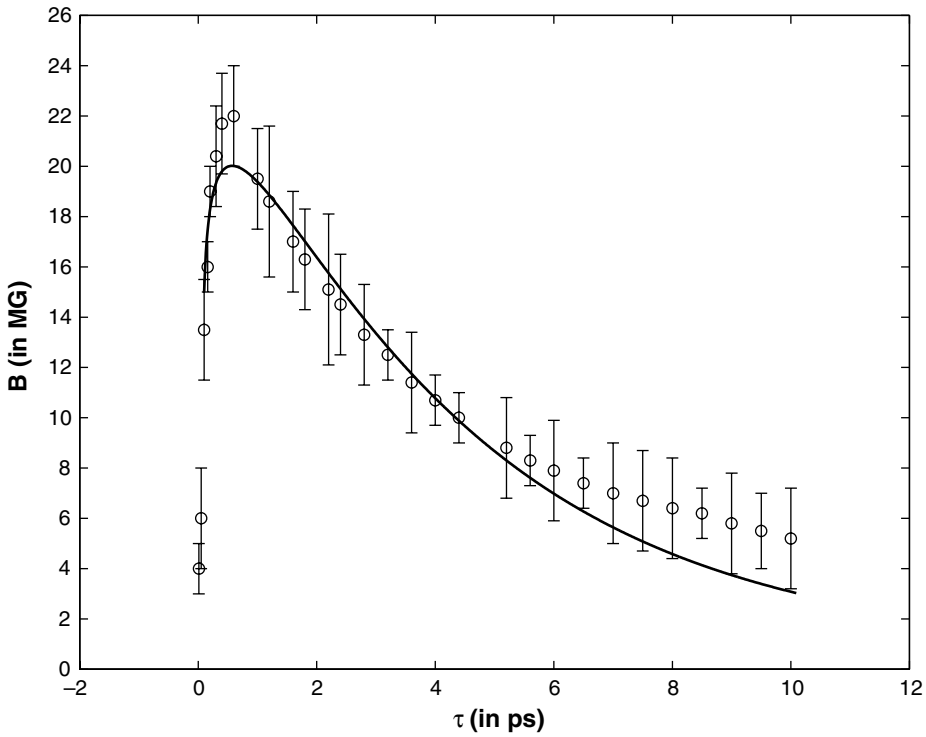

Figure 9. Magnetic field as a function of τ for the aluminium target.

the target normal. It is a 'p' polarized laser with an intensity of $\sim 10^{20}$ W m^{-2}. The duration of the pump pulse is 100 fs and its wavelength is 800 nm. The probe laser is incident normal to the target. The frequency of the probe beam is twice the frequency of the pump. Its intensity, is however, $\sim 10^3$ times weaker than the intensity of the pump beam. The probe, being at twice the frequency of the pump, can penetrate the target much beyond the critical density layer for the pump beam. It thus samples the overdense region in which hot electron currents produced by the pump beam propagate and cause the generation of quasi-static magnetic fields.

In our experiment we have measured the ellipticity induced in the probe pulse due to the quasi-static magnetic field (see figure 8). This measurement is carried out as a function of the time delay τ between the pump and the probe pulse. The measured ellipticity is transformed into magnetic field data by numerically studying the propagation of an electromagnetic wave through an inhomogeneous plasma. The wave vector of the electromagnetic wave would be perpendicular to the magnetic field direction as shown in figure 8. We have chosen an exponential density profile which expands at the sound speed corresponding to $T_e = 100$ eV and $Z = 5$ [12] for our analysis. We observe that the results are reasonably insensitive to the choice of density profile used in the numerical analysis. This method has been used earlier for a temporally resolved measurement of Mega-Gauss magnetic fields [13]. The plots of magnetic field for solid aluminium target and BK7 glass coated with aluminium layer as a function of time delay are shown in figures 9 and 10, respectively.

The circles represent experimental points and the solid curves, which show a reasonable fit, are obtained using a one-dimensional model developed below. We observe that, in both the cases, the measured magnetic field initially rises, goes to a maximum and decays exponentially. The point to note here is that the timescale of decay in glass is an order of magnitude smaller than in aluminium, indicating different mechanisms of anomalous stopping in dielectric (glass) and conductor (aluminium). Decay time in each case is related to the electrical resistivity (either electrostatically or turbulence induced) of the background plasma. Since our interest lies in anomalous stopping of the hot electron current after it is generated by the incident laser, we have modelled the experimental data beyond the time $t > \tau_{\text{laser}}$ using a formalism developed by Bell *et al* [14].

3.2. Theoretical modelling and analysis of data

The temporal evolution of magnetic field is modelled using the following equation, which describes the mechanism of quasi-static magnetic field generation under EMHD approximation [13]

$$\frac{\partial \vec{B}}{\partial t} = \frac{c^2}{4\pi\sigma}\nabla^2\vec{B} + \frac{c}{\sigma}(\nabla \times \vec{j}_{\text{hot}}). \tag{5}$$

The first term here describes the magnetic field decay due to resistive damping of the plasma shielding currents (σ being the conductivity of the background plasma) and the second term describes the magnetic field generation due to hot electron currents. Since the magnetic field generated in our experiments would be typically in the azimuthal direction (see the schematic of figure 8), the above equation is approximated to a scalar evolution equation in one dimension as given below.

$$\frac{\partial B}{\partial t} = -\frac{B}{\tau_d} + S(z,t). \tag{6}$$

Here the diffusion term has been modelled as B/τ_d with $\tau_d = (4\pi\sigma/c^2)(\Delta r)^2$, and the source term is approximated

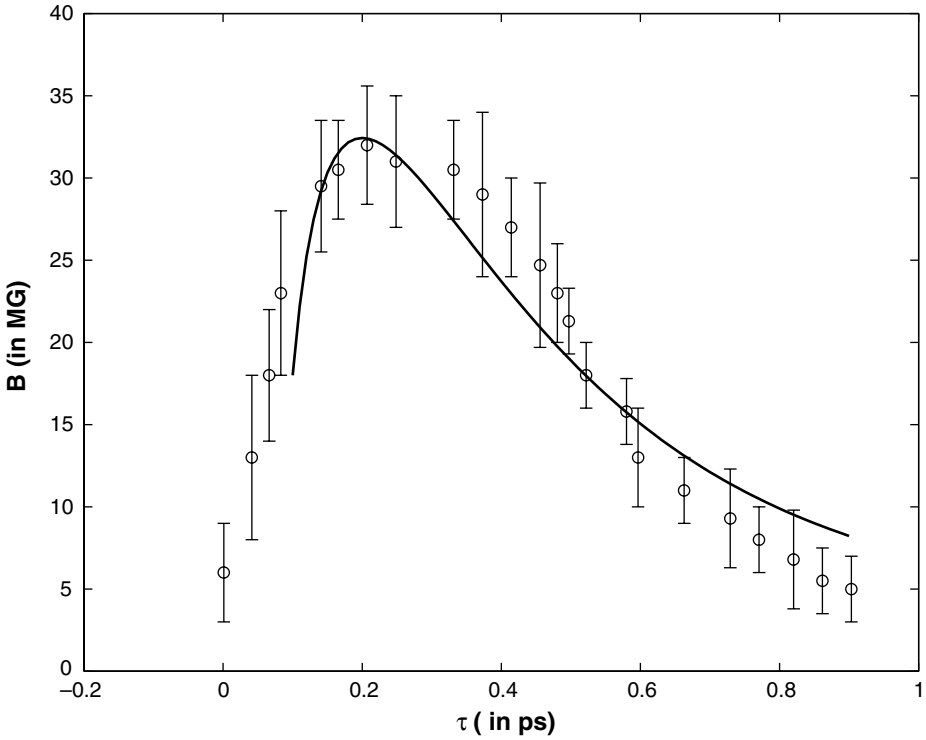

Figure 10. Magnetic field as a function of τ for the aluminium-coated glass target.

as $S(z,t) = -(c/\sigma(\Delta r))\, j_{\rm hot}(z,t)$. Here Δr is the laser spot radius, which is about 10 μm. Taking $B = B_{\rm las}$ at $t = \tau_{\rm laser}$, the solution is given by

$$B = B_{\rm las}\exp\left[-\left(\frac{t-\tau_{\rm laser}}{\tau_{\rm d}}\right)\right] - \exp\left[-\frac{t}{\tau_{\rm d}}\right] \times \int_{\tau_{\rm laser}}^{t} \frac{c}{\sigma\,\Delta r}\, j_{\rm hot}(z,t)\mathrm{e}^{(t/\tau_{\rm d})}\,\mathrm{d}t, \tag{7}$$

where $j_{\rm hot} = -en_{\rm h}v_{\rm h}$. Here $n_{\rm h}$ is the hot electron density and $v_{\rm h}$ is the velocity of the hot electron fluid. To make an estimate of $n_{\rm h}$ and $v_{\rm h}$, we use the formalism given by Bell *et al* [14]. According to Bell, the evolution of hot electron density $n_{\rm h}$ is governed by a nonlinear diffusion equation of the form

$$\frac{\partial n_{\rm h}}{\partial t} = \frac{\partial}{\partial z}\left[\frac{\sigma T_{\rm h}}{e^2}\frac{\partial n_{\rm h}}{\partial z}\right] \tag{8}$$

whose solution in the regime $t > \tau_{\rm laser}$ is given by

$$n_{\rm h} = \frac{2n_0 z_0}{\pi}\frac{L}{z^2+L^2} \tag{9}$$

with

$$L(t) = z_0\left[\frac{5\pi\sigma T_{\rm h}}{3e^2 n_0 z_0^2}(t-\tau_{\rm laser})+1\right]^{3/5}; \quad n_0 = \frac{2}{9}\frac{I_{\rm abs}^2\tau_{\rm laser}e^2}{\sigma T_{\rm h}^3}; \quad z_0 = \frac{3\sigma T_{\rm h}^2}{e^2 I_{\rm abs}}. \tag{10}$$

Here $T_{\rm h}$ is the hot electron temperature and the absorbed intensity $I_{\rm abs} = f I_{\rm incident}$, f being the fraction absorbed. The density of hot electrons is n_0 at $z = 0$ at time $t = \tau_{\rm laser}$ and z_0 is the characteristic stopping length such that $n_0 z_0$ is the total number of hot electrons produced at time $t = \tau_{\rm laser}$. The solution of the nonlinear diffusion equation is a self-similar solution in which the spatial shape remains the same but it expands in time with a scale length $L(t)$. Using the expressions for $n_{\rm h}$ and $L(t)$ we estimate $j_{\rm hot}$ as

$$j_{\rm hot} = -e\frac{2n_0 z_0}{\pi}\frac{L}{z^2+L^2}\left[\alpha\frac{\mathrm{d}L}{\mathrm{d}t}\right],$$

where $v_{\rm h}$, the hot electron velocity, is taken to be proportional to $\mathrm{d}L/\mathrm{d}t$, α being the proportionality constant. Substituting the expression for $\mathrm{d}L/\mathrm{d}t$ in $j_{\rm hot}$ and using it in equation (7) along with $\sigma = c^2/(4\pi(\Delta r)^2)\tau_{\rm d}$, we get

$$B = B_{\rm las}\exp[-y] + A\exp[-y]\tau_{\rm d}\int_0^y \frac{(py\tau_{\rm d}+1)^{1/5}\exp(y)}{z^2+z_0^2(py\tau_{\rm d}+1)^{6/5}}\mathrm{d}y, \tag{11}$$

where $y = (t-\tau_{\rm laser})/\tau_{\rm d}$, $A = (2cz_0\alpha T_{\rm h})/(e\Delta r)$ and $p = (5\pi\sigma T_{\rm h})/(3e^2 n_0 z_0^2)$. We now use the above expression for $B(t,z)$ at $z = 0$ to model the magnetic field evolution, as a function of time, for both BK7 glass coated with aluminium and solid aluminium. The model makes use of $\tau_{\rm d}$ (which is related to conductivity σ) and f (fraction of light absorbed) as free parameters. The point $z = 0$ is the location where hot electrons are generated. Hence $z = 0$ corresponds to the critical density point. The proportionality constant α is chosen as unity. The magnetic field $B_{\rm las}$ at time $t = \tau_{\rm laser}$ is 15 MG and 18 MG, respectively, for aluminium and glass targets. The best-fit curves (solid lines) are shown in figures 9 and 10, for which the relevant parameters (f and $\tau_{\rm d}$) for aluminium and glass are $f = 0.48$, $\tau_{\rm d} = 3.5$ ps and $f = 0.21$, $\tau_{\rm d} = 0.2$ ps, respectively. From the results of the fit, it is clear that the time for magnetic field decay in aluminium is an order of magnitude larger than in glass. Calculation of resistivity, using $\eta = (4\pi(\Delta r)^2)/(c^2\tau_{\rm d})$, gives $\eta_{\rm Al} = 3.6\times10^{-5}\,\Omega$–m and $\eta_{\rm glass} = 6.3\times10^{-4}\,\Omega$–m.

We see that the resistivity of aluminium as deduced from these measurements is an order of magnitude higher than the value of resistivity evaluated by Milchberg *et al* [12]. This provides evidence of turbulence induced anomalous resistivity in our experiments on aluminium targets. In the case of glass, our measurements show that neutralization of hot electron current is not as effective as it is in aluminium. This is due to high background resistivity, which results in inhibition of hot electron propagation in glass through generation of large electrostatic fields. Our modelling of the experimental data for the case of glass thus clearly demonstrates that in this case the anomalously fast stopping of hot electrons occurs because of electrostatic inhibition. The concept of anomalous resistivity may be of significance to the FI scheme of laser fusion, as can be seen from the following argument. As stated in the introduction, to ignite the spark the core has to be heated to a temperature of 10 keV within 10 ps. Considering only ohmic heating which is due to cold return currents [15] and using a hot electron density of $\sim 10^{27}\,\mathrm{m}^{-3}$ (this is the critical density for 1 μm wavelength laser), it can be shown that the resistivity needed to satisfy the ignition criterion is approximately three orders of magnitude higher than the Spitzer resistivity at 10 keV [16]. There already exists indirect evidence of such anomalously high resistivity in real fusion scale experiments [1, 2].

4. Summary and conclusions

In this work, we have presented experimental/theoretical results concerning the generation of hot electrons which are produced when an ultrashort high intensity laser pulse falls on a solid target and their subsequent propagation through the overdense plasma. Our study, firstly, shows that energetic electrons are produced at the critical surface via wave breaking of large amplitude plasma waves which are resonantly driven at the critical surface by the incident laser beam. And secondly, the propagation of hot electrons through the overdense region is significantly affected by electrostatically induced and/or turbulence induced resistivity. Further, as already pointed out in earlier sections, we believe that these experimental results, although obtained at non-relativistic intensities ($eE/m\omega c \ll 1$), may have relevance to FI physics.

References

[1] Kodama R. *et al* 2001 *Nature* **412** 798
[2] Kodama R. *et al* 2002 *Nature* **418** 933
[3] Von Der Linde D. *et al* 1992 *IEEE J. Quantum Electron.* **28** 2388
[4] Gizzi L.A. *et al* 1996 *Phys. Rev. Lett.* **76** 2278
[5] Kruer W.L. 1988 *The Physics of Laser–Plasma Interactions* (New York: Addison-Wesley)
[6] Erokhin N.S. *et al* 1969 *Sov. Phys.—JETP* **29** 101
[7] Milchberg H.M. *et al* 1989 *J. Opt. Soc. Am.* B **6** 1351
[8] Das A. *et al* 2001 *Phys. Plasmas* **8** 4518
[9] Jain N. *et al* 2003 *Phys. Plasmas* **10** 29
[10] Jain N. *et al* 2004 *Phys. Plasmas* **11** 4390
[11] Sentoku Y. *et al* 2003 *Phys. Rev. Lett.* **90** 155001-1
[12] Milchberg H.M. *et al* 1988 *Phys. Rev. Lett.* **61** 2364
[13] Sandhu A.S. *et al* 2002 *Phys. Rev. Lett.* **89** 225002-1
[14] Bell A.R. *et al* 1997 *Plasma Phys. Control. Fusion* **39** 653
[15] Davies J.R. 2003 *Phys. Rev.* E **68** 056404
[16] Sandhu A.S. *et al* Real time study of the fast electron transport inside dense, hot plasmas *Phys. Rev. Lett.* submitted

AQ4

QUERIES

Page 1
AQ1
In the first line of the introduction, we have added ‘fusion’ after ‘inertial confinement’ to complete the expansion of (ICF) and also as has been given in the first line of the abstract. Please confirm if this is ok.

Page 4
AQ2
Please check whether the edits made to the sentence ‘For this purpose.....plasma media’ retains the intended meaning.

Page 8
AQ3
We have changed all instances where ‘μ’ has been used as a unit micron/micrometre to ‘μm’. Please confirm if this is ok.

Page 9
AQ4
Please provide year, volume number and page range for reference [16].